Applied Clay Science 202 (2021) 105962

Contents lists available at ScienceDirect

Applied Clay Science

journal homepage: www.elsevier.com/locate/clay

Research Paper

The significant role of montmorillonite on the formation of hematite nanoparticles from ferrihydrite under heat treatment

Lixia Yan [a,b,c], Qingze Chen [a,c,*], Yixuan Yang [a,b,c], Runliang Zhu [a,b,c]

[a] CAS Key Laboratory of Mineralogy and Metallogeny/Guangdong Provincial Key Laboratory of Mineral Physics and Materials, Guangzhou Institute of Geochemistry, Chinese Academy of Sciences(CAS), Guangzhou 510640, China
[b] University of Chinese Academy of Sciences, Beijing 100049, China
[c] Institutions of Earth Science, Chinese Academy of Sciences, Beijing 100029, China

ARTICLE INFO

Keywords:
Mineral nanoparticles
Ferrihydrite
Montmorillonite
Hematite
Heat treatment
Size

ABSTRACT

With high surface reactivity and weak crystallinity, ferrihydrite (Fh) tends to be transformed to other thermodynamically stable iron (hydr)oxides, and its transformation is strongly influenced by the coexisting substances. Clay minerals widely coexist with Fh in the near-surface areas, but there is limited information about their effects on the transformation of Fh. In this work, the effect of montmorillonite (Mt) on the formation of hematite (Hem) nanoparticles from Fh under heat treatment was studied. Fh, Mt, and their mixed samples (Fh-Mt) were heated at different temperatures (350, 450, 600, 700, and 800 °C) for various times (3, 5, and 10 h), and the samples before and after heating were well characterized. X-ray diffraction and ^{57}Fe Mössbauer spectroscopy results revealed that Fh was transformed to Hem after heat treatment in both the presence and absence of Mt. Scanning electron microscopy and transmission electron microscopy images indicated that Mt could well disperse Fh and distinctly decrease the particle sizes of the formed Hem after heating. In particular, the particle size of Hem reached ~1000 nm in the pure Fh system, while it was only 15–75 nm in the systems containing Mt. Fourier transform infrared spectroscopy patterns displayed the strong interactions between Mt and Fh (through the formation of Si−O−Fe and Al−O−Fe bonds), which may also reduce the aggregation of Fh and inhibit the phase transformation of Fh particles into large Hem particles. This work verifies the important protective effect of clay minerals on coexisting iron oxide under high-temperature conditions, which would contribute to better understanding the formation and preservation of natural nano-sized minerals (particles) in nature.

1. Introduction

Nanominerals and mineral nanoparticles have attracted widespread attention during the last few decades, due to their unique atomic, electronic, and magnetic structures, physical and chemical behaviors, and reactivity comparative to the bulk minerals (Banfield and Zhang, 2001; Buseck and Adachi, 2008; Glenn et al., 2008; Hochella et al., 2008; Waychunas and Zhang, 2008; Hochella Jr et al., 2019). In the natural environment, the nanosized mineral would be gradually transformed to micro- and macro-scope mineral by consuming enough time, high energy, and needed components (e.g., ions, atoms, molecules) (Banfield and Zhang, 2001; De Yoreo et al., 2015), leading to the change of the special geochemical and mineralogical features. For example, the decreased reactivity of these nanominerals could greatly affect the fixation, transport, and fate of the coexisting substances (e.g., metal cations) (Petosa et al., 2010; Vindedahl et al., 2016). Therefore, studying the formation and retention of nanominerals and mineral nanoparticles are continuously drawing the interests of scientists.

Ferrihydrite (Fh), a metastable iron oxyhydroxide nanomineral with weak crystallinity and small particle size (2–6 nm), has been regarded as an ideal candidate for studying the transformation of mineral nanoparticles in the natural environment (Jambor and Dutrizac, 1998; Cornell and Schwertmann, 2003; Vodyanitskii, 2010). It has been revealed that high temperature and neutral pH favor the transformation of Fh to hematite (Hem) by dehydration-aggregation, while high or low pH promote the formation of goethite (Gth) through dissolution-recrystallization in aqueous systems (Das et al., 2011; Francisco et al., 2016; Yan et al., 2020). Besides, the effects of coexisting

* Corresponding author at: CAS Key Laboratory of Mineralogy and Metallogeny/Guangdong Provincial Key Laboratory of Mineral Physics and Materials, Guangzhou Institute of Geochemistry, Chinese Academy of Sciences(CAS), Guangzhou 510640, China.
E-mail address: chenqingze@gig.ac.cn (Q. Chen).

https://doi.org/10.1016/j.clay.2020.105962
Received 30 July 2020; Received in revised form 24 December 2020; Accepted 26 December 2020
Available online 10 January 2021

substances on the phase transformation of Fh aroused widespread concerns in recent years, many studies showed that metal cations, organic/inorganic anions, and natural organic matters inhibited the phase transformation of Fh (Li et al., 2020; Lu et al., 2019), nanosized substances showed various effects on Fh transformation depending on their interactions in aqueous system (e.g., graphene oxide inhibited Fh transformation while fullerol accelerated the transformation process) (Yan et al., 2020). By contrast, Fh is generally transformed to Hem under dry condition. The transformation process and the features of the formed Hem are complex, which greatly depend on various factors (e.g., temperature, time, and coexisting substances) (Campbell et al., 1997; Campbell et al., 2002; Burton et al., 2019b). For example, the crystal size of Hem increased from 24 nm (340 °C) to 700 nm (995 °C) by dry heat treatment of Fh, and could even reach micro-level (>1 um) by continuously increasing temperature (Stanjek, 1992; Campbell et al., 2002; Rzepa et al., 2016). The coexisting Si could promote the transformation temperature of Fh from 300−350 °C to 740 °C (molar ratio of Si/(Si + Fe) = 0.27), and also change the morphology and size of the transformation product (i.e., Hem) (Campbell et al., 2002; Rzepa et al., 2016); whereas the reductants (e.g., glucose) could cause the formation of magnetite and/or maghemite by heating Fh above 300 °C (Campbell et al., 1997). Most of the coexisting substances mentioned above, e.g., anions, cations, and organic matters, were in tiny size, and they usually affected the thermal transformation process by covering the surface sites of Fh, entering its structure, and reducing structural Fe (Carlson and Schwertmann, 1981; Campbell et al., 2002; Burton et al., 2019a; Burton et al., 2019b). In contrast, nanominerals and minerals nanoparticles with special nano-sized structure, large surface area, and high reactivity, are omnipresent in the environment (Banfield and Zhang, 2001; Hochella Jr et al., 2019), and may show individual effects on the transformation of Fh, which are important in the near-surface area, yet largely overlooked.

Clay minerals, the most ubiquitous nanominerals, always coexist with iron (oxyhydr)oxides nanoparticles in soils and sediments (Zhang et al., 2012; Zhou et al., 2012; Zeng et al., 2020). Previous studies demonstrated that clay minerals can inhibit the transformation of Fh to Hem/Gth under hydrothermal conditions through physical separation, bonding effect, and/or structural substitution (Celis et al., 1998; Schwertmann et al., 2000), leading to the preservation of Fh nanoparticles. However, less attention has been paid to the effect of coexisting clay minerals on the thermal transformation of Fh under dry conditions, although some natural (e.g., wildfire and volcano eruption) and man-made (e.g., straw burning) high temperature conditions are frequently happened on global scale (Burton et al., 2019a, 2019b; Certini, 2014). Theoretically, clay minerals could disperse Fh, which may accelerate the dehydration of Fh, and favor the formation of Hem. On the other hand, the layers of clay minerals may protect Fh from dehydration/dehydroxylation, and inhibit the subsequent phase transformation. Besides, the bonding effect between clay minerals and Fh may influence the particle size of the transformation products. As such, it is necessary to investigate how clay minerals affect the transformation of Fh and the formation of Hem under high-temperature conditions.

In this work, montmorillonite (Mt) was selected as a representative of clay minerals to study the effect on the thermal transformation process and product of Fh. The preservation effect of Mt on Hem nanoparticles in the vibration environment was also investigated by acidly treating the heating product of Fh and Mt mixture. Samples were characterized by X-ray diffraction (XRD), scanning electron microscope (SEM), transmission electron microscope (TEM), Mössbauer spectrum (MS), and Fourier transform infrared spectroscopy (FTIR). The characterization results indicated that the particle size of the transformation products (i.e., Hem) was obviously reduced by the coexisting Mt, suggesting a protective effect of clay minerals (i.e., Mt) on iron mineral nanoparticles. This work could provide novel information for the formation and preservation of mineral nanoparticles in the near-surface areas, especially in the natural and man-made high temperature environments.

2. Material and method

2.1. Materials

The original calcium-rich Mt (Ca−Mt) used in this study was highly pure (purity>95%) and was from Inner Mongolia, China (Chen et al., 2017; He et al., 2020). NaCl, $Fe(NO_3)_3{\cdot}9H_2O$, NaOH, and HNO_3 used were of analytical degree and were bought from Aladdin Chemistry Co. Ltd. All of the chemicals were used without further treatments.

2.2. Synthesis of modified Mt, Fh, and Fh-Mt mixtures

Na−Mt shows better dispersion than Ca−Mt in water and thus can help better disperse Fh particles. Herein, Na-exchanged Mt was used in this work. Na-exchanged Mt (hereafter named Na−Mt) was prepared according to the following procedures: Ca−Mt was dispersed in a 0.5 M of NaCl solution and was continuously stirred in a water bath at 60 °C for 24 h. The same operation was repeated three times for the complete exchange of Ca. The final suspension was centrifuged and washed using ultrapure water until Cl^- free (tested by $AgNO_3$) (Chen et al., 2016; Chen et al., 2017). The obtained Na−Mt was freeze-dried and sealed for the following experiments.

Fh was synthesized according to the method of Cornell and Schwertmann (2003). In brief, $Fe(NO_3)_3{\cdot}9H_2O$ and NaOH were titrated to pH 7-8 with continuously stirring. Subsequently, the suspension was centrifuged and washed repeatedly with ultrapure water to remove the remanent chemicals. After being freeze-dried for 48 h, the obtained Fh was sealed and refrigerated for further usage.

The mixed samples of Fh-Mt were synthesized in water for sufficient mixing. Briefly, Mt was firstly put in water and ultrasonically treated 30 min for uniform dispersing. Then, different contents of Fh were added into Mt suspensions under continuously stirring, and the samples were named as Fh-Mt*a* ($a = 0.5, 1, 5$ depending on the initial mass ratio of Mt/Fh. For example, Fh-Mt0.5 represents the mass ratio of Mt/Fh = 0.5, and the content of Mt in the system is 33.3%). The pH of the mixed suspensions was adjusted to 6 (± 0.5) with 0.1 M NaOH and 0.1 M HNO_3. After constantly stirred for 48 h at room temperature, the suspensions were filtrated by a suction filter, and the obtained solids were freeze-dried for the following analyses.

2.3. Thermal treatment of Mt, Fh, and Fh-Mt mixtures

The thermal treatment process was conducted in air. Typically, Fh, Mt, and the mixed samples of Fh-Mt were placed in corundum crucibles and then heated at 350, 450, 600, 700, and 800 °C for different times (i.e., 3, 5, and 10 h). The thermally treated samples were denoted as Fh-Mt*a*-temperature-time (e.g., Fh-Mt5-800-10 represents the sample of Fh-Mt5 being heated at 800 °C for 10 h). The heating temperatures were selected according to the range of temperatures that occur in surface soils during a wildfire (Certini, 2005; Johnston et al., 2016; Burton et al., 2019a; Johnston et al., 2019), and the heating times were selected to better investigate the effects of Mt on the transformation of Fh.

2.4. Acid treatment of the heating product of Fh-Mt mixture

The heating product of Fh-Mt mixture (i.e., Fh-Mt5-800-10) was acidly treated in the vibration environment to investigate the preservation effect of Mt on the nano-sized products. 0.1 g of the sample was put in 25 mL of ultrapure water, and the pH of the suspension was adjusted to 3 using 0.1 M HNO_3 and 0.1 M NaOH. Subsequently, the suspension was continuously stirred at room temperature (25 °C) and 200 rpm for 30 days, and was washed twice with ultrapure water to remove the impurities. The sample was dispersed for TEM analysis.

2.5. Analytical methods

XRD patterns of the samples were obtained on a Bruker D8 Advance X-ray diffractometer (Karlsruhe, German) with a Ni-filtered Cuka radiation. The measurements were conducted at 40 mA and 40 kV, and the patterns were recorded over the 2θ range of 3–70° at a scanning rate of 3°/min.

Zeta potentials measurements were performed at room temperature using a Zetasizer Nano-ZS90 instrument (UK). 0.05 g of each sample (i.e., Fh, Mt, Fh-Mt5) was added into 20 mL ultrapure water under continuous stirring. The pH was adjusted from 3 to 10 using 0.1 M HNO_3 and 0.1 M NaOH.

SEM images were obtained using a Carl Zeiss Supra 55 field emission scanning electron microscope. The powder samples before and after heat treatment were added on a conducting resin holding by the holder.

TEM images were obtained by an FEI Talos F200S transmission electron microscope with an accelerating voltage of 200 kV. A drop of the highly dispersed suspension (dispersed by ultrasonic treatment) was dropped on a Cu pane and was air-dried for analysis.

FTIR spectra were obtained with a PerkinElmer spectrometer. Samples for measurement were prepared by pressing a mixture of 50 mg KBr and 0.5 mg sample powders to disks. All of the samples were recorded ranging from 4000 and 400 cm^{-1} with a resolution of 4 cm^{-1} and 64 interferograms.

MS was measured at room temperature in the transmission mode operating in constant acceleration mode using a WSS-10 instrument. A ^{57}Co in the Rh matrix was used as the Mössbauer source. Quantitative analysis of the spectra was conducted using the *MossWinn* program.

3. Result and discussion

3.1. Characterizations of Fh, Mt, and Fh-Mt mixtures before heating

3.1.1. XRD analysis

XRD patterns of Fh, Mt, and the mixed samples before heating were recorded (Fig. 1a). Two broad reflections at $2\theta = 36°$ and 63°, matching well with the standard pattern of two-line Fh, were observed in the XRD pattern of Fh (Cornell and Schwertmann, 2003; Yan et al., 2020). As for Mt, the d_{001}-value of 1.25 nm suggested the good exchange of Ca^{2+} by Na^{+} (the d_{001}-value of Ca−Mt being 1.51 nm) (Chen et al., 2017). For Fh-Mt mixtures, the intensity of the characteristic reflections of Mt was low in the samples of Fh-Mt0.5, which may be attributed to the interaction between Fh and the basel/edges of Mt, causing the unordered stack of Mt layers during the drying process (Celis et al., 1998; Fan et al., 2009). The poor orientation of Mt was relieved by decreasing the value of Fh/Mt from 2 to 1 and then to 1/5. Besides, no other mineral phase was found in the mixed samples, indicating that the mixing process did not induce the phase transformation of Fh.

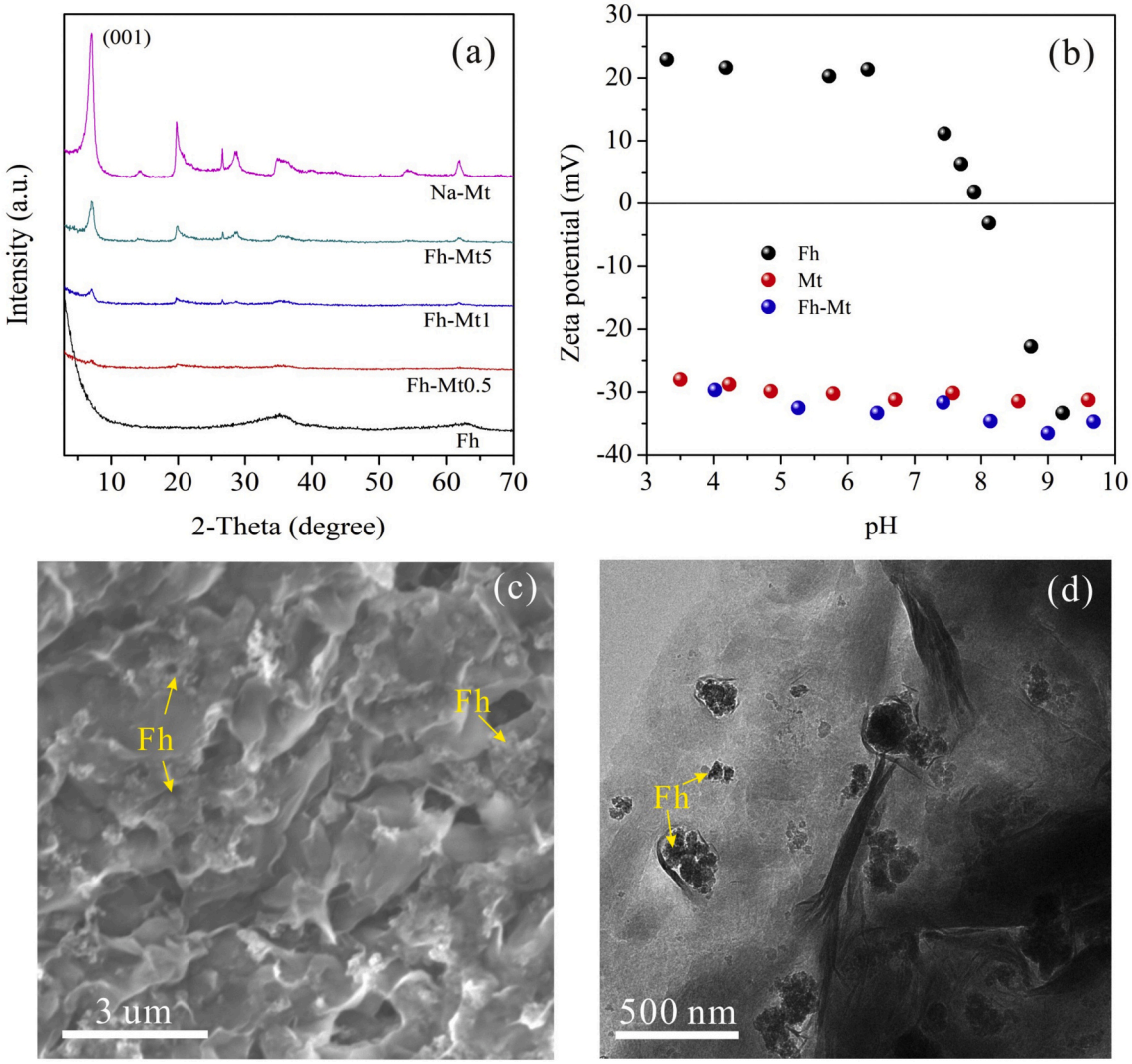

Fig. 1. Information of the Fh-Mt mixtures before thermal treatment. XRD (a), Zeta potential (b), SEM image of Fh-Mt5 (c), and TEM image of Fh-Mt5 (d).

3.1.2. Zeta potential

Results of zeta potentials showed that the pH of the zero point of charge (pH_{zpc}) of Fh was ~8 (Fig. 1b), consistent with the results from the previous studies (Liu et al., 2016; Liu et al., 2017). The decreasing of the zeta potential with raising the pH could be due to the change of the adsorbed ions (i.e., H^+ and OH^-) (Cornell and Schwertmann, 2003). According to the previous studies, the sheet of Mt has permanent negative charges due to the high structural substitution of Al^{3+} for Mg^{2+} and Fe^{2+} in the octahedron, as well as the substitution of Si^{4+} for Al^{3+} in the tetrahedron (Cui et al., 2020; Zarzycki et al., 2007). The change of pH may change the features of the edge −OH, but the content of these −OH is small (~10%) (Zarzycki et al., 2007). So the surface charge of Mt was dominated by the sheet, and the pH-independent of the permanent negative charge resulted in the constant of zeta potential with increasing solution pH. Otherwise, the zeta potential values of Mt were close to −30 mV in the range of 3–10, indicating a good dispersion of Mt in water because of the electrostatic repulsion (Zhao et al., 2015; Chen et al., 2016), which favored the electrostatic attraction between Mt and Fh particles in the mixing process at pH 6. In addition, the similar zeta potential of Mt with Fh-Mt may be due to the high content of Mt (83.3%) in the mixture sample.

3.1.3. Morphology characterization

SEM and TEM images showed that Mt was lamellar mineral with randomly distributed pores (Fig. S1). As for the Fh-Mt mixture, Fh particles and small aggregates were dispersed in the pores, surfaces, and edges of Mt lamellas (Fig. 1c and d). As is well known, Fh particles commonly exist as large aggregates at near-neutral pH due to their low surface charges and large surface energy (Banfield et al., 2000; Cismasu et al., 2011). In the mixed system, however, Mt could disperse Fh and inhibit the formation of large aggregates, which was coincident with the previous study showing the good dispersion effects of Mt on the coexisting nanoparticles (e.g., iron nanoparticles) (Fan et al., 2018).

3.1.4. FTIR spectroscopy analysis

FTIR spectra were collected to investigate the interaction between Fh and Mt (Fig. S2), and the assignments of the adsorption bands were summarized (Table S1). The adsorption band at 3618 cm^{-1} was attributed to the stretching vibration mode of Al−OH in Mt (Chen et al., 2017; Shu et al., 2019; Qiao et al., 2020). The bands of 3421–3436 and 1628–1635 cm^{-1} were the stretching and bending vibration of the adsorbed H_2O, respectively (Chen et al., 2017; Shu et al., 2019). The Fe−O (1503 cm^{-1}) and Fe−OH (1351 cm^{-1}) bands were inconspicuous in Fh-Mt5, which may be caused by the low crystallinity and content of Fh (Liu et al., 2017). Additionally, the obvious deviations of the complex Si−O stretching bands (from 978, 1022, 1113, and 1190 cm^{-1} for Mt to 990, 1037, 1105, and 1185 cm^{-1} for Fh-Mt5, respectively) were ascribed to the interaction between Fh and the Si−OH of Mt (Mahmoud et al., 2015; Pentrak et al., 2018; Shu et al., 2019). The adsorption bands at 690 and 910 cm^{-1} were respectively assigned to the Al–O stretching and Al−OH bending vibrations in Mt. The shift of the adsorption bands from 910 to 906 cm^{-1} in the sample of Fh-Mt5 may be caused by the formation of Al−O−Fe bond between Fh and the terminal Al−OH of Mt (Liu et al., 2013; Shu et al., 2019).

3.2. Characterizations of Fh, Mt, and Fh-Mt mixtures after heating

3.2.1. XRD analysis

XRD patterns of the thermal transformation products verified that the heating transformation products of Fh were Hem under the selected heating temperatures (i.e., 350, 450, 600, 700, and 800 °C) (Fig. S3a). Besides, the intensity of the characteristic reflections of Hem increased and the corresponding full width at half maximum (FWHM) decreased with raising the heating temperature (Table S2), which indicated that larger sized Hem with better crystallinity was obtained at a higher temperature (Sorensen et al., 2000; Masina et al., 2015; Vithana et al., 2018). As for Mt (Fig. S3b), the intensity of d_{001} reflection decreased with raising the heating temperature, and the interlayer space of Mt collapsed at 600 °C for 10 h, which was confirmed by the decrease of the basal spacing from 1.25 to 0.97 nm (Balek et al., 2006; Chen et al., 2017). After heating at 800 °C for 10 h, a broad reflection belonging to an amorphous phase of $MgAl_2O_4$-SiO_2 solid was observed in the XRD pattern, suggesting the removal of the structural hydroxyls of Mt under the high-temperature condition (Chen et al., 2017).

For the mixed sample (Fh-Mt5), the characteristic reflections of Mt disappeared gradually with rising the temperature and time, and an amorphous phase of $MgAl_2O_4$-SiO_2 was obtained at 800 °C for 10 h (Fig. 2a), which was consistent with the result for pure Mt (Fig. S3b). Besides, Hem was the only transformation product of Fh in these Fh-Mt mixture samples, suggesting that the coexisting Mt could not change the product mineral type of Fh.

The effects of various contents of Mt on the phase transformation of Fh were further investigated, and the corresponding XRD patterns showed that the reflection intensities of Hem decreased with increasing Mt content (Fig. 2b). Compared with the heating product of Fh (i.e., Fh-800-10), these mixtures exhibited the wider FWHM of Hem reflections (Table S2). The above results indicated that increasing Mt contents could reduce the crystallinity and particle size of Hem. Here, the mean sizes of Hem particles in these systems were calculated using the Scherrer equation based on the XRD patterns (Yuan et al., 2008; Mokoena et al., 2017), and the calculation details were shown in the *Supplementary materials*. The obtained results showed that the average sizes for the systems of Fh-Mt5, Fh-Mt1, and Fh-Mt0.5 were 21 ± 0.12, 25 ± 0.33, and 32 ± 0.13 nm, respectively (Table S3), which further confirmed that the particle size of Hem increased with decreasing Mt content.

3.2.2. Morphology and size analysis

SEM was used to observe the morphologies and sizes of the products of Mt and Fh after heat treatment (Fig. 3a-b). The product of Mt kept the similar lamellar shape to raw Mt (< 2 um) (Fig. S1), and Hem particles showed the morphology of granular under different heating conditions (heating at 450, 600, and 800 °C for 10 h, or 800 °C for 3, 5, and 10 h) (Fig. S4 and S5). Moreover, the particle sizes of Hem increased with raising the heating temperature and time, consistent with the previous studies about the aging of iron (hydr)oxides by heating treatment (Sorensen et al., 2000; Cornell and Schwertmann, 2003). In particular, the particle size of Fh-800-10 reached ~1000 nm (Fig. 3a), obviously larger than the Hem in other tested systems with various temperatures and heating times (Figs. S4 and S5). In the mixed systems, Hem aggregates and particles were distributed on the surfaces and edges of the lamellas, as well as the porous spaces among different layers (Fig. 3c-e). Besides, the content of Hem aggregates decreased with increasing the mass ratio of Mt/Fh, and the particle sizes of Hem (< 100 nm) were evidently smaller than that (~1000 nm) in the system of Fh-800-10 (Fig. 3).

These interpretations were further verified by TEM analysis. Hem in the control system was granular particles (Fig. 4a), and the product of Mt kept the lamellar shape (Fig. 4b). The introduction of Mt showed no evident impact on the morphologies of Hem (Fig. 4c–f). Unlike the diamond and/or hexagon texture of the Hem particles formed at the hydrothermal environment (Schwertmann et al., 2000; Das et al., 2011; Echigo et al., 2012), the granular morphologies of Hem at the dry-heating condition may be attributed to the fast dehydration of Fh aggregates and the subsequent growth at high-temperature condition. However, the particle sizes of Hem were evidently influenced by Mt (Fig. 4). In particular, the sizes of Hem in the systems containing Mt (<100 nm) were significantly smaller than those in the pure Fh system (~1000 nm), consistent with the XRD and SEM results above. As described in the previous studies, Mt was a good dispersing agent for positively charged coexisting substances (e.g., iron nanoparticles), due to its negatively charged surface (zeta potential < −30 eV) and large sheet (Yuan et al., 2008; Fan et al., 2009; Chen et al., 2016; Fan et al.,

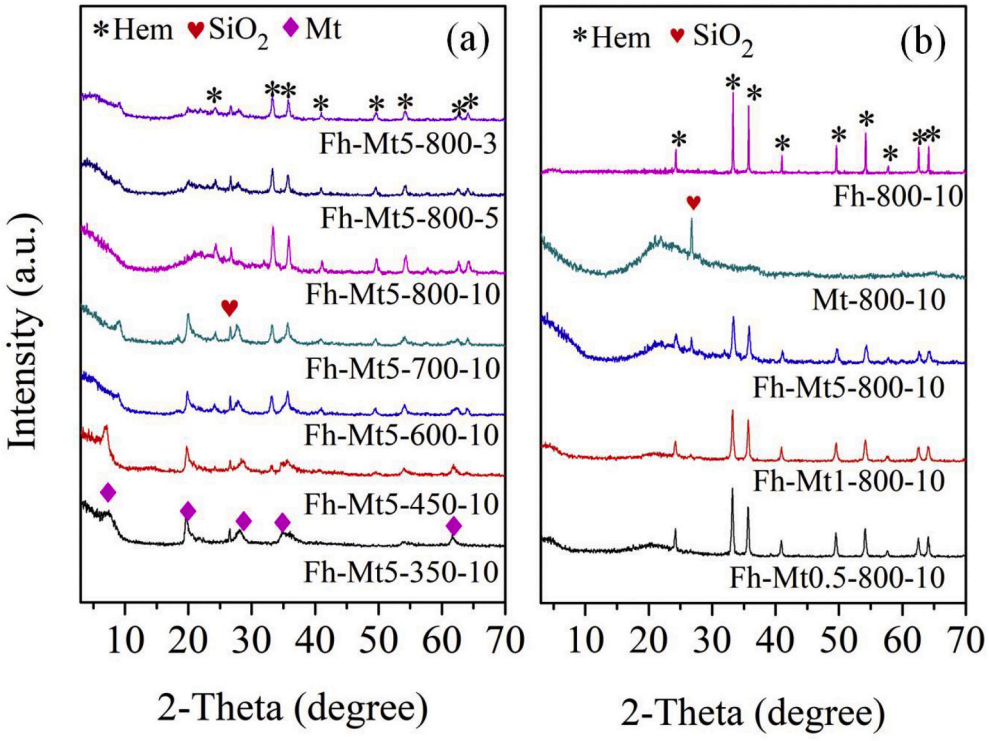

Fig. 2. XRD pattern of heat-treated Fh-Mt5 at different temperatures and times (a); XRD pattern of samples with different Fh/Mt ratios after heating at 800 °C for 10 h (b).

2018). Likewise, in this work, Fh could be well dispersed by Mt under continuously stirring in water. As a result, the contact and aggregation of Fh particles were inhibited, which facilitates the generation of small Hem particles.

The size distributions of Hem in the mixture systems were obtained by measuring 50 of Hem particles based on the TEM images. The particle sizes distributions patterns showed that the sizes of Hem particles became uneven gradually with decreasing Mt contents (Fig. 4c-e). The average size of Hem increased from 25 nm for Fh-Mt5 to 27 nm for Fh-Mt1, and 37 nm for Fh-Mt0.5 (Fig. 4c-e and Table S3), agreed well with the above XRD results. The increasing average size of Hem may be attributed to the increasing contact among Fh particles resulted from the decreasing contents of Mt (Schwertmann et al., 2000). HRTEM pattern showed the interplanar distance of 0.37 nm (Fig. 4f) belonging to the (012) plane of Hem (Patra et al., 2015), which further confirmed the formation of Hem after heat treatment of Fh-Mt.

3.2.3. MS measurement

MS patterns of Fh-800-10, Mt-800-10, and Fh-Mt5-800-10 were collected to further investigate the effect of Mt on the transformation product of Fh (Fig. 5), and the fitted parameters of these systems were listed (Table 1). The pattern of Fh-800-10 was fitted to a sextet with parameters of isomer shift (IS) = 0.37 mm/s, quadrupole splitting (QS) = −0.21 mm/s, and magnetic hyperfine field (B_{HF}) = 52.01 T (Table 1 and Fig. 5a), indicating the formation of Hem (Cornell and Schwertmann, 2003; Jacob and Khadar, 2010). The MS of Mt-800-10 was fitted to two doublets (Fig. 5b). The fitting parameters of IS = 0.32 mm/s and QS = 0.92 mm/s were assigned to the Si−O−Fe phase in the poorly ordered lamellar heating product (Campbell et al., 2002; Hu et al., 2019). The parameters of IS = 0.21 mm/s and QS = 0.53 mm/s were ascribed to the amorphous Al−O−Fe phase (Labatut et al., 1998) (Hu et al., 2019).

As for Fh-Mt5-800-10, a sextet and two doublets were obtained (Fig. 5c). The fitted parameters of the sextet corresponded to the Fe^{3+} site in the structure of Hem, and no other iron (hydro)oxide phases were obtained (Table 1), further confirming that Mt could not change the product type of Fh. Interestingly, the B_{HF} value of the Fh-Mt5-800-10 (50.76 T) was smaller than that (52.01 T) in the sample of Fh-800-10. Lemine et al. (2010) investigated the MS features of Hem particles with different sizes, and demonstrated that the B_{HF} value of Hem with a particle size of 10 nm (49.2 T) was smaller than that (B_{HF} = 51.3 T) in an 80 nm Hem particle (Lemine et al., 2010). Similarly, the smaller B_{HF} value of Fh-Mt5-800-10 (compared with that of Fh-800-10) in this study should be attributed to the smaller particle size of the former. On the other hand, the doublet was determined as a mixture of Si−O−Fe (IS = 0.30 mm/s and QS = 0.92 mm/s) and slight Al−O−Fe (IS = 0.21 mm/s and QS = 0.53 mm/s) phases with a content ratio of 19.81/1.88 (Table 1), which was larger than that of Mt-800-10 (88.45/11.55). This result may be attributed to the more interaction between the Fe−OH with the marginal Si−OH during the mixing and heating process (Campbell et al., 2002; Hu et al., 2019).

3.2.4. FTIR spectroscopy characterization

FTIR spectra of the heat-treated samples were compared (Fig. 6 and Table S1). The spectrum corresponding to the sample of Fh-800-10 displayed the absorption bands at 480 and 559 cm^{-1}, which were assigned to the characteristic absorption bands of Fe−O in the Hem phase (Fig. 6a) (Nathan and Boby, 2017; Zhang et al., 2020). In the spectrum of Mt-800-10, an amorphous phase of $MgAl_2O_4$-SiO_2, showed adsorption bands at 467 cm^{-1} for the Si−O−Si bending mode, at 796 and 1051–1211 cm^{-1} for the Si−O stretching vibration. Besides, the bands of 913 and 971 cm^{-1} were ascribed to the Al−O bending vibration from marginal Al−Al−OH and the stretching vibration of Si−OH, respectively (Fig. 6b) (Liu et al., 2013; Fedel et al., 2014; Rzepa et al., 2016; Chen et al., 2017).

As for Fh-Mt5-800-10, the stretching vibration of Fe−O at the band of 555 cm^{-1} was observed (Fig. 6a), confirming the presence of Hem. The adsorption bands at 913 (Al−O stretching) and 971 (Si−O stretching) cm^{-1} on the spectrum of Mt-800-10 were respectively shifted to 907 and 959 cm^{-1} in Fh-Mt5-800-10, which could be due to the formation of

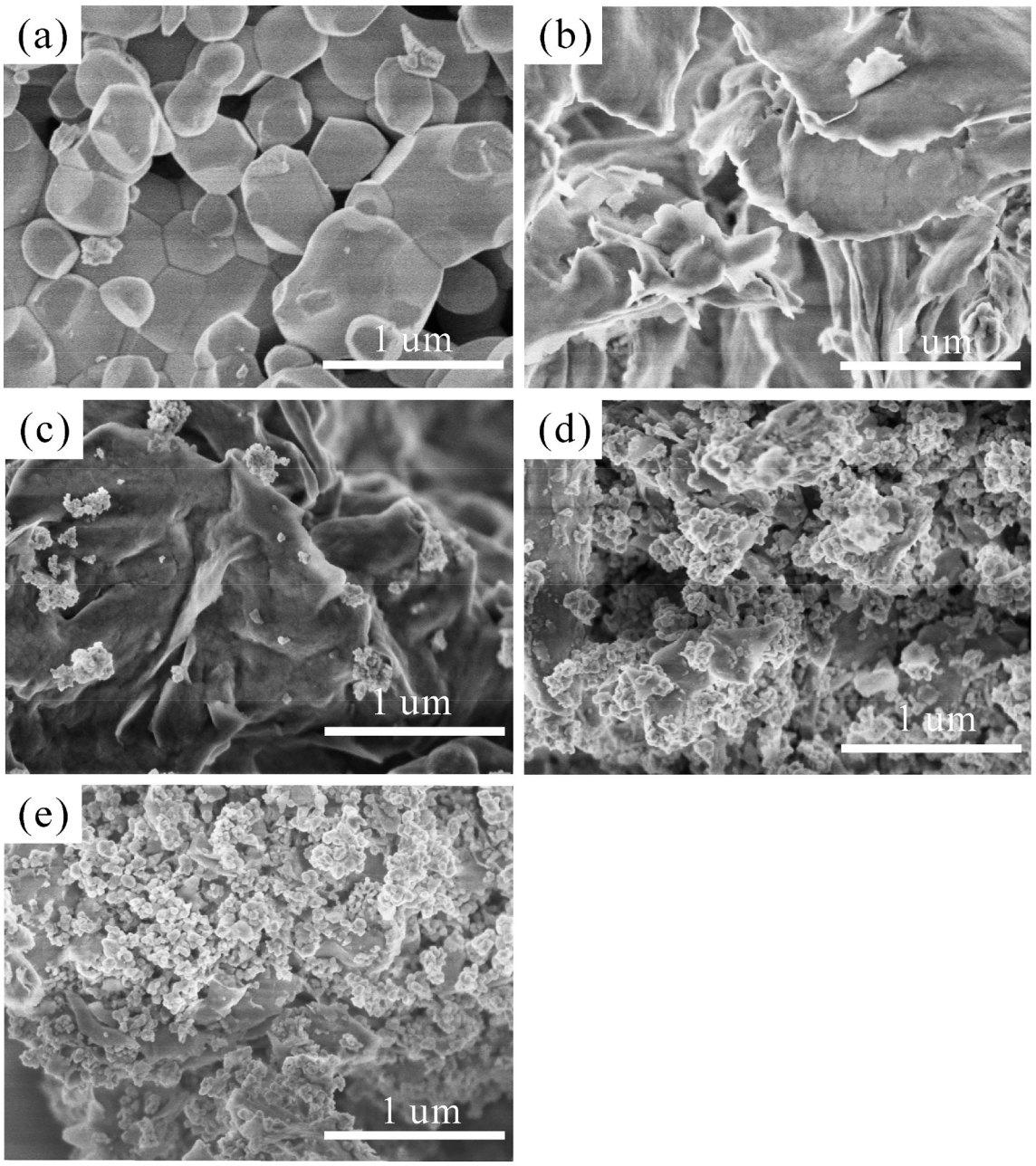

Fig. 3. SEM images of the thermal-treated products of Fh, Mt, and Fh-Mt mixture samples after heating at 800 °C for 10 h. Fh-800-10 (a), Mt-800-10 (b), Fh-Mt5-800-10 (c), Fh-Mt1-800-10 (d), and Fh-Mt0.5-800-10 (e).

Al−O−Fe and Si−O−Fe through the interaction between the Fe−OH of Fh with the Al−OH and Si−OH of Mt during the heating process (Emmanuel et al., 2001; Shu et al., 2019; Zhang et al., 2020). Similar results were presented by Shu et al. (2019), who investigated the formation process of schwertmannite on Mt, and indicated the formation of Si−O−Fe and Al−O−Fe bond between the marginal Si−OH/Al−OH of Mt and Fe−OH from schwertmannite (Shu et al., 2019). Furthermore, the shift of Si−O stretching vibration band (from 1051, 1142, and 1211 to 1043, 1130, and 1206 cm^{-1}, respectively) may also be connected to the formation of Si−O−Fe (Emmanuel et al., 2001; Mahmoud et al., 2015; Pentrak et al., 2018; Zhao et al., 2018).

3.3. Mechanism analysis

Fh nanoparticles prone to accumulate due to their nanosize and high surface energy, and the aggregates tend to transform to Hem in high temperature conditions through dehydroxylation and structural rearrangement. The obtained results (Figs. S4 and S5) in our study showed that the particle size of Hem increased with raising the heating temperature and time. Fh exists extensively in the near-surface area, generally in the form of thin films that coating the clay minerals (e.g., Mt) (Jones Angela, 1987; Zeng et al., 2020). Due to the high surface reactivity, clay minerals are expected to affect the transformation process and product features (e.g., size and morphology) of Fh. For example, Schwertmann et al. (2000) found that allophone and soil smectite can evidently decrease the phase transformation rate of Fh in aqueous system at room temperature and pH 4-7. In our study, Fh and Mt were well mixed in an aqueous phase, and the dry heating results showed that the particle size of Hem (~1000 nm) in the Mt containing systems were evidently larger than the contron system (15–75 nm).

Several characterization methods were used to explore the significant effect of Mt on the formation of Hem nanoparticles. Zeta potential

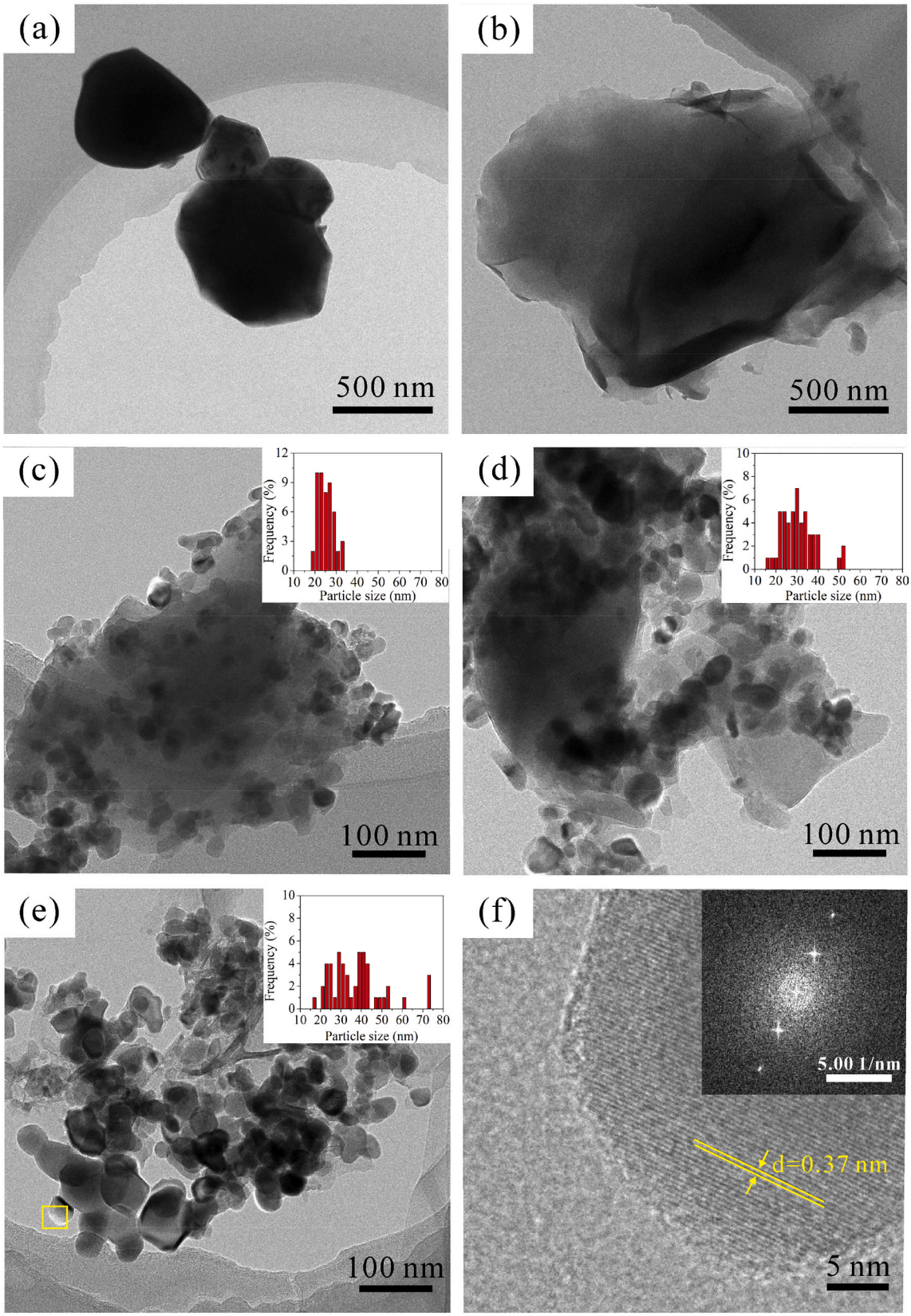

Fig. 4. TEM images of the thermal-treated products of Fh-Mt mixture samples after heating at 800 °C for 10 h. Fh-800-10 (a), Mt-800-10 (b), Fh-Mt5-800-10 (c), Fh-Mt1-800-10 (d), and Fh-Mt0.5-800-10 (e), the enlarge area of the yellow box of e (f).ion of the references to colour in this figure legend, the reader is referred to the web version of this article.)

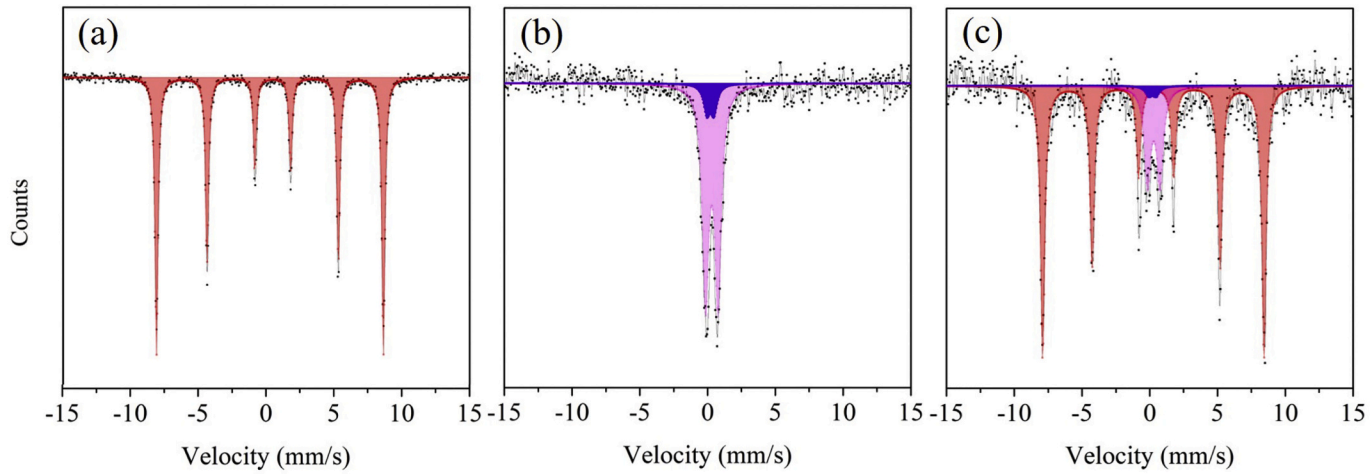

Fig. 5. Mössbauer spectra of Fh-800-10 (a), Mt-800-10 (b), and Fh-Mt5-800-10 (c). Red area: Hem; Purple area: Si−O−Fe phase; Blue area: Al−O−Fe phase. (For interpretation of the references to colour in this figure legend, the reader is referred to the web version of this article.)

Table 1
Room temperature Mössbauer fitting parameters of different samples. (IS: isomer shift, QS: quadrupole splitting, and B_{HF}: internal hyperfine splitting).

Sample name	IS (mm/s)	QS (mm/s)	B_{HF} (T)	Content (%)	Phase
Fh-800-10	0.37	−0.21	52.01	100	Hematite
Mt-800-10	0.32	0.92	–	88.45	Si−O−Fe
	0.21	0.53	–	11.55	Al−O−Fe
Fh-Mt5-800-10	0.37	−0.21	50.76	78.31	Hematite
	0.30	0.92	–	19.81	Si−O−Fe
	0.21	0.53	–	1.88	Al−O−Fe

results demonstrated that Fh and Mt were oppositely charged and could contact by electrostatic attraction (Fig. 1b). SEM and TEM results showed that Fh particles/aggregates were dispersed well on the surface and pores structure of Mt sheets (Fig. 1c and d). Besides, FTIR results indicated that Fh and Mt could interact through the bonding effect between Al−OH/Si−OH of the end faces of Mt and Fh (i.e., forming Si−O−Fe and Al−O−Fe) (Fig. 6 and S2). As such, several reasons may simultaneously contribute to the formation of Hem nanoparticles: (1) the lamellar Mt could form a porous structure (e.g., card-house-like structure), and disperse Fh via physical separation; (2) the formation of Si−O−Fe and Al−O−Fe bonds between Fh and Mt (via the ligand exchange between Fe–OH and Si–OH/Al–OH) could well immobilize Fh nanoparticles, and thus limit the formation of large Fh aggregates (Fig. 7). It is generally recognized that phase transformation mechanism of Fh to Hem was aggregation and dehydration. However, both of the interaction between Mt and Fh showed above inhibited the aggregation process, so that the phase transformation of Fh and the formation of large sized Hem were hampered. The obtained results of this study help to understand the phase transformation of Fh in naural and man-made high temperature conditions, and provide novel ideas for the formation and protective of mineral nanopartices in the near surface environment.

In addition to the influence of the particle size of Hem, the coexisting substances may alter the morphology of Hem particles (Cornell and

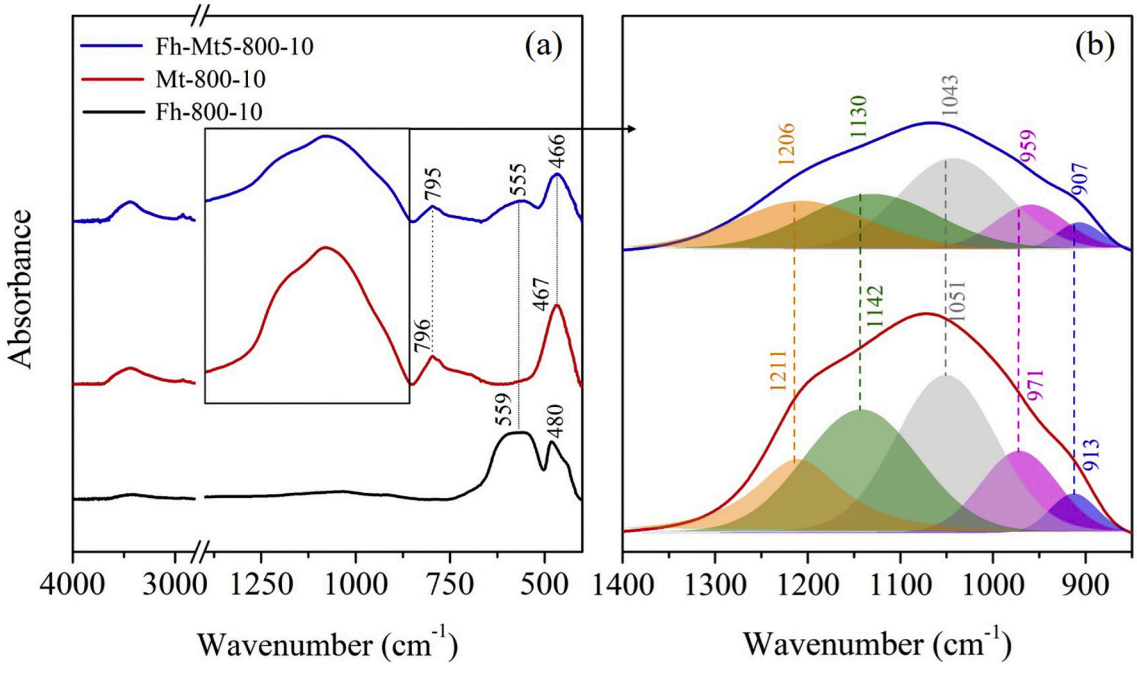

Fig. 6. FTIR spectra of Fh-800-10, Mt-800-10, and Fh-Mt5-800-10 (a). The enlarged view of the spectra in the range of 850–1400 cm^{-1} (b).

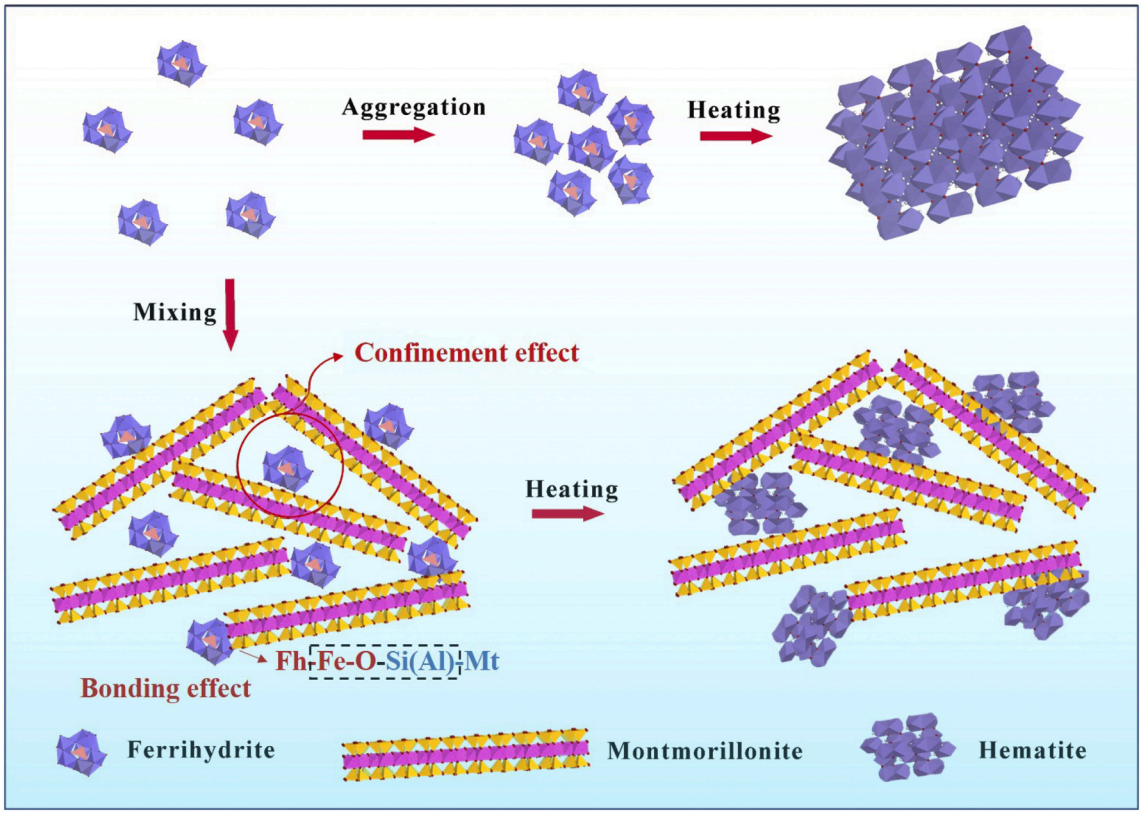

Fig. 7. Schematic drawing of the transformation processes of Fh in different systems.

Schwertmann, 2003; Vodyanitskii, 2010). For instance, Schwertmann et al. (2000) proposed that the transformation product (i.e., Hem) were circular/ellipsoidal shape in the pure Fh system at acid aqueous condition (pH 4), while it changed to pseudo-hexagonal plates in the presence of clay minerals, due to the preferential adsorption of the dissolved ions (i.e., Al, Si) on the specific surfaces of Hem (Schwertmann et al., 2000). In our study, no ions (e.g., Al and Si) were dissolved from Mt and preferentially adsorbed on the surface of Hem in the mixing process of Fh and Mt (pH 6), so that the morphology of the transformation product (i.e., Hem) was quite similar in the systems with and without Mt.

3.4. Migration behavior of Hem nanoparticles in the Fh-Mt mixture sample under shanking and acidic condition

Above results showed that Mt could favor the formation of Hem nanoparticles at high-temperature conditions. One would wonder whether the Hem nanoparticles could be released from the porous structure and edges (Si−O−Fe/Al−O−Fe) of Mt under natural/artificial violent shock (e.g., earthquake and agricultural practice) or acid conditions (e.g., acid soil, acid mine drainage). Here, the sample of Fh-Mt5-800-10 was stirred continuously under acidic pH condition (i.e., pH 3), and the TEM results showed that some Hem nanoparticles could be released from the lamellar heating product of Fh-Mt5 (i.e., Fh-Mt5-800-10) in shanking and acidic condition (Fig. S6). In this sense, clay minerals (e.g., Mt) may not only serve as storages for the formation and protection of nanoparticles, but also as a “nano-factory” that can provide nanoparticles continuously for the near-surface environments.

4. Conclusions

In this study, the effect of Mt on the thermal transformation of Fh was investigated. Our results verified that the transformation product of Fh after heat treatment only consisted of Hem. The coexisting Mt could not change the types of the transformation product, but evidently decreased the particle size of the formed Hem, owing to the structure of the confined space and the fixed action of the hydroxyls on the end face of Mt. This study identifies the protective effect of Mt on Hem nanoparticles under high-temperature conditions. It is noteworthy that the natural condition is complex, and other coexisting substances (e.g., metal cations, and inorganic ions) could influence the interaction between Mt and Fh, further interfering with the transformation process and products of Fh. Therefore, more detailed studies on the influence of Mt on the thermal transformation of Fh are needed. Also, the effects of other clay minerals with various morphologies and structural features (e.g., kaolinite and palygorskite) on the heat transformation of Fh will be further studied.

Declaration of Competing Interest

The authors declare that they have no known competing financial interests or personal relationships that could have appeared to influence the work reported in this paper.

Acknowledgments

This is contribution No. IS-2960 from GIGCAS. This work was financially supported by the National Natural Science Foundation of China (grant No. 41872044, 41902040), Youth Innovation Promotion Association CAS (grant No. 2020347), CAS Interdisciplinary Innovation Team (grant No. JCTD-2019-15), Science and Technology Planning of Guangdong Province (grant No. 2020B1212060055). The authors also thank Dr. J. Liu from Guangzhou Institute of Geochemistry, Chinese Academy of Sciences for the valuable suggestions.

Appendix A. Supplementary data

Supplementary data to this article can be found online at https://doi.org/10.1016/j.clay.2020.105962.

References

Balek, V., Benes, M., Malek, Z., Matuschek, G., Kettrup, A., Yariv, S., 2006. Emanation thermal analysis study of Na-montmorillonite and montmorillonite saturated with various cations. J. Therm. Anal. Calorim. 83, 617–623.

Banfield, J.F., Zhang, H., 2001. Nanoparticles in the environment. Rev. Mineral. Geochem. 44, 1–58.

Banfield, J.F., Welch, S.A., Zhang, H., Ebert, T.T., Lee, P.R., 2000. Aggregation-based crystal growth and microstructure development in natural iron oxyhydroxide biomineralization products. Science 289, 751–754.

Burton, E.D., Choppala, G., Karimian, N., Johnston, S.G., 2019a. A new pathway for hexavalent chromium formation in soil: fire-induced alteration of iron oxides. Environ. Pollut. 247, 618–625.

Burton, E.D., Choppala, G., Vithana, C.L., Karimian, N., Hockmann, K., Johnston, S.G., 2019b. Chromium(VI) formation via heating of Cr(III)-Fe(III)-(oxy)hydroxides: a pathway for fire-induced soil pollution. Chemosphere 222, 440–444.

Buseck, P.R., Adachi, K., 2008. Nanoparticles in the atmosphere. Elements 4, 389–394.

Campbell, A.S., Schwertmann, U., Campbell, P.A., 1997. Formation of cubic phases on heating ferrihydrite. Clay Miner. 32, 615–622.

Campbell, A.S., Schwertmann, U., Stanjek, H., Friedl, J., Kyek, A., Campbell, P.A., 2002. Si incorporation into hematite by heating Si-ferrihydrite. Langmuir 18, 7804–7809.

Carlson, L., Schwertmann, U., 1981. Natural ferrihydrites in surface deposits from Finland and their association with silica. Geochim. Cosmochim. Acta 45, 421–429.

Celis, R., Cornejo, J., Hermosin, M.C., 1998. Textural properties of synthetic clay-ferrihydrite associations. Clay Miner. 33, 395–407.

Certini, G., 2005. Effects of fire on properties of forest soils: a review. Oecologia 143, 1–10.

Certini, G., 2014. Fire as a soil-forming factor. Ambio 43, 191–195.

Chen, Q.Z., Zhu, R.L., Zhu, Y.P., Liu, J., Zhu, L.F., 2016. Adsorption of polyhydroxy fullerene on polyethylenimine-modified montmorillonite. Appl. Clay Sci. 132-133, 412–418.

Chen, Q.Z., Zhu, R.L., Ma, L.Y., Zhou, Q., Zhu, J.X., He, H.P., 2017. Influence of interlayer species on the thermal characteristics of montmorillonite. Appl. Clay Sci. 135, 129–135.

Cismasu, A.C., Michel, F.M., Tcaciuc, A.P., Tyliszczak, T., 2011. Composition and structural aspects of naturally occurring ferrihydrite. Compt. Rendus Geosci. 343, 210–218.

Cornell, R.M., Schwertmann, U., 2003. The Iron Oxides: Structure, Properties, Reactions, Occurrences, and Uses, second edition. Wiley-VCH.

Cui, J.R., Zhang, Z.P., Han, F., 2020. Effects of pH on the gel properties of montmorillonite, palygorskite and montmorillonite-palygorskite composite clay. Appl. Clay Sci. 190, 105543.

Das, S., Hendry, M.J., Essilfie-Dughan, J., 2011. Transformation of two-line ferrihydrite to goethite and hematite as a function of pH and temperature. Environ. Sci. Technol. 45, 268–275.

De Yoreo, J.J., Gilbert, P.U.P.A., Sommerdijk, N.A.J.M., Penn, R.L., Whitelam, S., Joester, D., Zhang, H., Rimer, J.D., Navrotsky, A., Banfield, J.F., 2015. Crystallization by particle attachment in synthetic, biogenic, and geologic environments. Science 349, aaa6760.

Echigo, T., Aruguete, D.M., Murayama, M., Hochella Jr., M.F., 2012. Influence of size, morphology, surface structure, and aggregation state on reductive dissolution of hematite nanoparticles with ascorbic acid. Geochim. Cosmochim. Acta 90, 149–162.

Emmanuel, Doelsch, William, E., Stone, E., Sabine, Petit, Armand, Masion, 2001. Speciation and crystal chemistry of Fe(III) chloride hydrolyzed in the presence of SiO_4 ligands. 2. Characterization of Si-Fe aggregates by FTIR and ^{29}Si solid-state NMR. Langmuir 17, 1399–1405.

Fan, M.D., Yuan, P., Zhu, J.X., Chen, T.H., Yuan, A.H., He, H.P., Chen, K.M., Liu, D., 2009. Core-shell structured iron nanoparticles well dispersed on montmorillonite. J. Magn. Magn. Mater. 321, 3515–3519.

Fan, M.D., Wang, R.Z., Jia, S.Y., Xing, H.Y., Yang, Q., Jia, Z.H., 2018. Controllable synthesis of iron nanoparticles on polyethylenimine-modified montmorillonite: dependence on the amine protonation extent. Appl. Clay Sci. 162, 418–427.

Fedel, M., Callone, E., Dire, S., Deflorian, F., Olivier, M.G., Poelman, M., 2014. Effect of Na-montmorillonite sonication on the protective properties of hybrid silica coatings. Electrochim. Acta 124, 90–99.

Francisco, P.C.M., Sato, T., Otake, T., Kasama, T., 2016. Kinetics of Fe^{3+} mineral crystallization from ferrihydrite in the presence of Si at alkaline conditions and implications for nuclear waste disposal. Am. Mineral. 101, 2057–2069.

Glenn, A., Waychunas, Hengzhong, Zhang, 2008. Structure, chemistry, and properties of mineral nanoparticles. Elements 4, 381–387.

He, Q.Z., Zhu, R.L., Chen, Q.Z., Zhu, Y.P., Yang, Y.X., Du, J., Zhu, J.X., He, H.P., 2020. One-pot synthesis of the reduced-charge montmorillonite via molten salts treatment. Appl. Clay Sci. 186, 105429.

Hochella Jr., M.F., Mogk, D.W., Ranville, J., Allen, I.C., Luther, G.W., Marr, L.C., McGrail, B.P., Murayama, M., Qafoku, N.P., Rosso, K.M., 2019. Natural, incidental, and engineered nanomaterials and their impacts on the Earth system. Science 363, 1414.

Hochella, M.F., Lower, S.K., Maurice, P.A., Penn, R.L., Sahai, N., Sparks, D.L., Twining, B. S., 2008. Nanominerals, mineral nanoparticles, and earth systems. Science 319, 1631–1635.

Hu, Y., Liang, S., Yang, J.K., Chen, Y., Ye, N., Ke, Y., Tao, S.Y., Xiao, K.K., Hu, J.P., Hou, H.J., Fan, W., Zhu, S.Y., Zhang, Y.S., Xiao, B., 2019. Role of Fe species in geopolymer synthesized from alkali-thermal pretreated Fe-rich Bayer red mud. Constr. Build. Mater. 200, 398–407.

Jacob, J., Khadar, M.A., 2010. VSM and Mössbauer study of nanostructured hematite. J. Magn. Magn. Mater. 322, 614–621.

Jambor, J.L., Dutrizac, J.E., 1998. Occurrence and constitution of natural and synthetic ferrihydrite, a widespread iron oxyhydroxide. Cheminform 98, 2549–2585.

Johnston, S.G., Burton, E.D., Moon, E.M., 2016. Arsenic mobilization is enhanced by thermal transformation of schwertmannite. Environ. Sci. Technol. 50, 8010–8019.

Johnston, S.G., Burton, E.D., Karimian, N., 2019. Fire promotes arsenic mobilization and rapid arsenic(III) formation in soil via thermal alteration of arsenic-bearing iron oxides. Front. Earth Sci. 7, 139.

Jones Angela, A., 1987. A study of the thickness of ferrihydrite coatings on kaolinite. Mineral. Mag. 51, 87–92.

Labatut, C., Berjoan, R., Armas, B., Schamm, S., Sevely, J., Roig, A., Molins, E., 1998. Studies of LPCVD Al-Fe-O deposits by XPS, EELS and Mössbauer spectroscopies. Surf. Coat. Tech. 105, 31–37.

Lemine, O.M., Sajieddine, M., Bououdina, M., Msalam, R., Mufti, S., Alyamani, A., 2010. Rietveld analysis and Mössbauer spectroscopy studies of nanocrystalline hematite alpha-Fe_2O_3. J. Alloy. Compd. 502, 279–282.

Li, Y., Yang, M.J., Pentrak, M., He, H.P., Arai, Y., 2020. Carbonate-enhanced transformation of ferrihydrite. Environ. Sci. Technol. 54, 13701–13708.

Liu, D., Yuan, P., Liu, H.M., Cai, J.G., Tan, D.Y., He, H.P., Zhu, J.X., Chen, T.H., 2013. Quantitative characterization of the solid acidity of montmorillonite using combined FTIR and TPD based on the NH_3 adsorption system. Appl. Clay Sci. 80-81, 407–412.

Liu, J., Zhu, R.L., Xu, T.Y., Xu, Y., Ge, F., Xi, Y.F., Zhu, J.X., He, H.P., 2016. Co-adsorption of phosphate and zinc(II) on the surface of ferrihydrite. Chemosphere 144, 1148–1155.

Liu, J., Zhu, R.L., Xu, T.Y., Laipan, M.W., Zhu, Y.P., Zhou, Q., Zhu, J.X., He, H.P., 2017. Interaction of polyhydroxy fullerenes with ferrihydrite: adsorption and aggregation. J. Environ. Sci. 64, 1–9.

Lu, Y., Hu, S.W., Wang, Z.M., Ding, Y., Lu, G.M., Lin, Z., Dang, Z., Shi, Z.Q., 2019. Ferrihydrite transformation under the impact of humic acid and Pb: kinetics, nano-scale mehcanisms, and implications for C and Pb dynamics. Environ. Sci. Nano 6, 747–762.

Mahmoud, H.H., Battisha, I.K., Ezz-Eldin, F.M., 2015. Structural, optical and magnetic properties of gamma-irradiated SiO_2 xerogel doped Fe_2O_3. Spectrochim. Acta A 150, 72–82.

Masina, C.J., Neethling, J.H., Olivier, E.J., Ferg, E., Manzini, S., Lodya, L., Mohlala, P., Ngobeni, M.W., 2015. Mechanism of reduction in hydrogen atmosphere and thermal transformation of synthetic ferrihydrite nanoparticles. Thermochim. Acta 599, 73–83.

Mokoena, T.P., Linganiso, E.C., Swart, H.C., Kumar, V., Ntwaeaborwa, O.M., 2017. Cooperative luminescence from low temperature synthesized alpha-Al_2O_3: Yb^{3+} phosphor by using solution combustion. Ceram. Int. 43, 174–181.

Nathan, D.M.G.T., Boby, S.J.M., 2017. Hydrothermal preparation of hematite nanotubes/reduced graphene oxide nanocomposites as electrode material for high performance supercapacitors. J. Alloy. Compd. 700, 67–74.

Patra, A.K., Kundu, S.K., Bhaumik, A., Kim, D., 2015. Morphology evolution of single-crystalline hematite nanocrystals: magnetically recoverable nanocatalysts for enhanced facet-driven photoredox activity. Nanoscale 8, 365–377.

Pentrak, M., Hronsky, V., Palkova, H., Uhlik, P., Komadel, P., Madejova, J., 2018. Alteration of fine fraction of bentonite from Kopernica (Slovakia) under acid treatment: a combined XRD, FTIR, MAS NMR and AES study. Appl. Clay Sci. 163, 204–213.

Petosa, A.R., Jaisi, D.P., Quevedo, I.R., Elimelech, M., Tufenkji, N., 2010. Aggregation and deposition of engineered nanomaterials in aquatic environments: role of physicochemical interactions. Environ. Sci. Technol. 44, 6532–6549.

Qiao, Z.C., Liu, Z.J., Zhang, S., Yang, Y.J., Wu, Y.K., Liu, L.H., Liu, Q.F., 2020. Purification of montmorillonite and the influence of the purification method on textural properties. Appl. Clay Sci. 187, 105491.

Rzepa, G., Pieczara, G., Gawel, A., Tomczyk, A., Zalecki, R., 2016. The influence of silicate on transformation pathways of synthetic 2-line ferrihydrite. J. Therm. Anal. Calorim. 2016, 407–421.

Schwertmann, U., Friedl, J., Stanjek, H., Schulze, D.G., 2000. The effect of clay minerals on the formation of goethite and hematite from ferrihydrite after 16 years' ageing at 25 degrees C and pH 4–7. Clay Miner. 35, 613–623.

Shu, Z.P., Liu, L.H., Qiu, G.H., Yang, X., Zhang, M.Z., Tan, W.F., Liu, C.S., Wu, F., 2019. Photochemical formation process of schwertmannite on montmorillonite and corresponding Cr(VI) adsorption capacity. ACS Earth Space Chem. 3, 718–727.

Sorensen, M.A., Stackpoole, M.M., Frenkel, A.I., Bordia, R.K., Korshin, G.V., Christensen, T.H., 2000. Aging of iron (hydr)oxides by heat treatment and effects on heavy metal binding. Environ. Sci. Technol. 34, 3991–4000.

Stanjek, H., 1992. The effect of dry heating on the chemistry, surface area, and oxalate solubility of synthetic 2-line and 6-line ferrihydrites. Clay Miner. 27, 397–411.

Vindedahl, A.M., Strehlau, J.H., Arnold, W.A., Penn, R.L., 2016. Organic matter and iron oxide nanoparticles: aggregation, interactions, and reactivity. Environ. Sci. Nano 3, 494–505.

Vithana, C.L., Johnston, S.G., Dawson, N., 2018. Divergent repartitioning of copper, antimony and phosphorus following thermal transformation of schwertmannite and ferrihydrite. Chem. Geol. 483, 530–543.

Vodyanitskii, Y.N., 2010. Iron hydroxides in soils: a review of publications. Eurasian Soil Sci. 43, 1244–1254.
Waychunas, G.A., Zhang, H., 2008. Structure, chemistry, and properties of mineral nanoparticles. Elements 4, 381–387.
Yan, L.X., Zhu, R.L., Liu, J., Yang, Y.X., He, H.P., 2020. Effects of fullerol and graphene oxide on the phase transformation of two-line ferrihydrite. ACS Earth Space Chem. 4, 335–344.
Yuan, P., Annabi-Bergaya, F., Tao, Q., Fan, M.D., Liu, Z.W., Zhu, J.X., He, H.P., Chen, T. H., 2008. A combined study by XRD, FTIR, TG and HRTEM on the structure of delaminated Fe-intercalated/pillared clay. J. Colloid Interface Sci. 324, 142–149.
Zarzycki, P., Szabelski, P., Piasecki, W., 2007. Modelling of zeta-potential of the montmorillonite/electrolyte solution interface. Appl. Surf. Sci. 253, 5791–5796.
Zeng, Q., Huang, L.Q., Ma, J.Y., Zhu, Z.H., Dong, H.L., 2020. Bio-reduction of ferrihydrite-montmorillonite-organic matter complexes: effect of montmorillonite and fate of organic matter. Geochim. Cosmochim. Acta 276, 327–344 (in press).
Zhang, C.X., Paterson, G.A., Liu, Q.S., 2012. A new mechanism for the magnetic enhancement of hematite during heating: the role of clay minerals. Stud. Geophys. Geod. 56, 845–860.
Zhang, Y., Qing, M., Wang, H., Liu, X.W., Liu, S., Wan, H., Li, L., Gao, X., Yang, Y., Wen, X.D., Li, Y.W., 2020. Comprehensive understanding of SiO_2-promoted Fe Fischer-Tropsch synthesis catalysts: Fe-SiO_2 interaction and beyond. Catal. Today (In press).
Zhao, J., Liu, F.F., Wang, Z.Y., Cao, X.S., Xing, B.S., 2015. Heteroaggregation of graphene oxide with minerals in aqueous phase. Environ. Sci. Technol. 49, 2849–2857.
Zhao, Y.L., Dong, F.Q., Dai, Q.W., Li, G., Ma, J., 2018. Variation of preserving organic matter bound in interlayer of montmorillonite induced by microbial metabolic process. Environ. Sci. Pollut. R. 25, 22348–22355.
Zhou, D.X., Abdelfattah, A.I., Keller, A.A., 2012. Clay particles destabilize engineered nanoparticles in aqueous environments. Environ. Sci. Technol. 46, 7520–7526.